Supporting Information for

Interdependence of cellular and network properties in respiratory rhythm generation

Ryan S. Phillips, and Nathan A. Baertsch

Ryan Phillips, Nathan Baertsch
E-mail: Ryan.Phillips@seattlechildrens.org, Nathan.Baertsch@seattlechildrens.org

This PDF file includes:

Supporting text
Figs. S1 to S15
Table S1
SI References

Supporting Information Text

Supplementary Methods.

Neuron Model. Model preBötC neurons include a single compartment and incorporate Hodgkin-Huxley style conductances adapted from previously described models (1–3) and/or experimental data as detailed below. The membrane potential of each neuron is governed by the following differential equation:

$$C\frac{dV}{dt} = -I_{Na} - I_K - I_{SPK} - I_{AHP} - I_{NaP} - I_{Ca} - I_{Leak} - I_{Tonic} - I_{Syn}, \quad [1]$$

where $C = 36\,pF$ is the membrane capacitance and each I_i represents a current, with i denoting the current's type. The currents include the action potential generating Na^+ and delayed rectifying K^+ currents (I_{Na} and I_K), a high voltage activated Na^+ and K^+ currents for augmenting spike amplitude (I_{SPK}) and AHP (I_{AHP}), a persistent Na^+ current (I_{NaP}), voltage-gated Ca^{2+} current (I_{Ca}), K^+ dominated leak current (I_{Leak}), a tonic excitatory synaptic current (I_{Tonic}) and a dynamic excitatory synaptic current (I_{Syn}) which mediates preBötC network interactions. The currents are defined as follows:

$$I_{Na} = g_{Na} \cdot m_{Na}^3 \cdot h_{Na} \cdot (V - E_{Na}) \quad [2]$$

$$I_K = g_K \cdot m_K^4 \cdot (V - E_K) \quad [3]$$

$$I_{SPK} = g_{SPK} \cdot m_{SPK} \cdot h_{SPK} \cdot (V - E_{Na}) \quad [4]$$

$$I_{AHP} = g_{AHP} \cdot m_{AHP} \cdot (V - E_K) \quad [5]$$

$$I_{NaP} = g_{NaP} \cdot m_{NaP} \cdot h_{NaP} \cdot (V - E_{Na}) \quad [6]$$

$$I_{Ca} = g_{Ca} \cdot m_{Ca} \cdot h_{Ca} \cdot (V - E_{Ca}) \quad [7]$$

$$I_{Leak} = g_{Leak} \cdot (V - E_{Leak}) \quad [8]$$

$$I_{Tonic} = g_{Tonic} \cdot (V - E_{Syn}) \quad [9]$$

$$I_{Syn} = g_{Syn} \cdot (V - E_{Syn}), \quad [10]$$

where g_i is the maximum conductance, E_i is the reversal potential, and m_i and h_i are gating variables for channel activation and inactivation for each current I_i. The glutamatergic synaptic conductance g_{Syn} is dynamic and is defined below (Eq. 18). The values used for the g_i and E_i appear in Table S1.

Table S1. Ionic Channel Parameters.

Channel	Parameters				
I_{Na}	$g_{Na} = 150\,nS$	$E_{Na} = 26.54 \cdot ln(Na_{out} = 120\,mM/Na_{in} = 15\,mM) \approx 55.188\,mV$			
	$m_{1/2} = -43.8\,mV$	$k_m = 6.0\,mV$	$\tau^m_{max} = 0.25\,ms$	$\tau^m_{1/2} = -43.8\,mV$	$k^m_\tau = 14.0\,mV$
	$h_{1/2} = -67.5\,mV$	$k_h = -11.8\,mV$	$\tau^h_{max} = 8.46\,ms$	$\tau^h_{1/2} = -67.5\,mV$	$k^h_\tau = 12.8\,mV$
I_K	$g_K = 220\,nS$	$E_K = 26.54 \cdot ln(K_{bath} = 8.5\,mM/K_{in} = 125\,mM) \approx -71.35\,mV$			
	$A_\alpha = 0.011$	$B_\alpha = 44.0\,mV$	$k_\alpha = 5.0\,mV$		
	$A_\beta = 0.17$	$B_\beta = 49.0\,mV$	$k_\beta = 40.0\,mV$		
I_{SPK}	$g_{SPK} = Variable$				
	$m_{1/2} = -27.5\,mV$	$k_m = 1\,mV$	$\tau_m = 0.5\,ms$		
	$h_{1/2} = -27.5\,mV$	$k_h = -1\,mV$	$\tau_h = 5\,ms$		
I_{AHP}	$g_{AHP} = Variable$				
	$m_{1/2} = -27.5\,mV$	$k_m = 1\,mV$	$\tau_m = 5\,ms$		
I_{NaP}	$g_{NaP} = N(\mu_{NaP}, \sigma_{NaP})$	$\mu_{NaP} = 3.33\,nS$	$\sigma_{NaP} = 0.75\,nS$		
	$m_{1/2} = -47.1\,mV$	$k_m = 3.1\,mV$	$\tau^m_{max} = 1.0\,ms$	$\tau^m_{1/2} = -47.1\,mV$	$k^m_\tau = 6.2\,mV$
	$h_{1/2} = -60.0\,mV$	$k_h = -9.0\,mV$	$\tau^h_{max} = 5000\,ms$	$\tau^h_{1/2} = -60.0\,mV$	$k^h_\tau = 9.0\,mV$
I_{Leak}	$g_{Leak} = N(\mu_{leak}, \sigma_{leak})$	$\sigma_{leak} = 0.05 \cdot \mu_{leak}$	$\mu_{leak} = exp((K_{Bath} - 3.425)/4.05)$		
	$E_{Leak} = -26.54 \cdot ln[(P_{Na} \cdot Na_{in} + P_K \cdot K_{in})/(P_{Na} \cdot Na_{out} + P_K \cdot K_{Bath})]$			$P_{Na} = 1$	$P_K = 42$
	$E_{Leak} \approx -63.73\,mV$				
I_{Tonic}	$g_{Tonic} = Variable$	$E_{Syn} = 0.0\,mV$			
I_{Syn}	$g_{Syn} = Dynamic$, See Eq. 18	$E_{Syn} = 0.0\,mV$	$\tau_{Syn} = 5.0\,ms$		

Activation (m_i) and inactivation (h_i) of voltage-dependent channels are described by the following differential equation:

$$\tau_X(V) \cdot \frac{dX}{dt} = X_\infty(V) - X; \quad X \in \{m, h\} \tag{11}$$

where X_∞ represents steady-state activation/inactivation and τ_X is a time constant. For I_{Na}, I_{NaP}, I_{Ca}, I_{SPK}, and I_{AHP}, the functions X_∞ and τ_X take the forms

$$X_\infty(V) = 1/(1 + \exp(-(V - X_{1/2})/k_X)), \tag{12}$$

$$\tau_X(V) = \tau^X_{max}/\cosh((V - \tau^X_{1/2})/k^X_\tau). \tag{13}$$

The values of the parameters ($X_{1/2}$, k_X, τ^X_{max}, $\tau^X_{1/2}$, and k^X_τ) corresponding to I_{Na}, I_{NaP},I_{Ca}, I_{SPK} and I_{AHP} are given in Table S1.

For I_K, steady-state activation $m^K_\infty(V)$ and time constant $\tau^K_m(V)$ are given by the expressions

$$m^K_\infty(V) = \alpha_\infty(V)/(\alpha_\infty(V) + \beta_\infty(V)), \tag{14}$$

$$\tau^K_m(V) = 1/(\alpha_\infty(V) + \beta_\infty(V)) \tag{15}$$

where

$$\alpha_\infty(V) = A_\alpha \cdot (V + B_\alpha)/(1 - \exp(-(V + B_\alpha)/k_\alpha)), \tag{16}$$

$$\beta_\infty(V) = A_\beta \cdot \exp(-(V + B_\beta)/k_\beta). \tag{17}$$

The values for the constants A_α, A_β, B_α, B_β, k_α, and k_β are also given in Table S1.

When we include multiple neurons in the network, we index them with subscripts. Then the total synaptic conductance $(g_{Syn})_i$ of the i^{th} target neuron is described by the following equation:

$$(g_{Syn})_i = g_{Tonic} + \sum_{j \neq i;n} W_{j,i} \cdot D_j \cdot C_{j,i} \cdot H(t - t_{j,n}) \cdot e^{-(t-t_{j,n})/\tau_{syn}}, \tag{18}$$

where $W_{j,i}$ represents the weight of the synaptic connection from neuron j to neuron i, D_j is a scaling factor for short-term synaptic depression in the presynaptic neuron j (described in more detail below), $C_{j,i}$ is an element of the connectivity matrix ($C_{j,i} = 1$ if neuron j makes a synapse with neuron i and $C_{j,i} = 0$ otherwise), $H(.)$ is the Heaviside step function, and t denotes time. τ_{Syn} is an exponential synaptic decay constant, while $t_{j,n}$ is the time at which the n^{th} action potential generated by neuron j reaches neuron i.

This model includes short-term synaptic depression motivated by experimental observations in the preBötC (4) and past computational models have suggested (5, 6). Synaptic depression in the j^{th} neuron (D_j) was simulated using an established mean-field model of short-term synaptic dynamics (7–9) as follows:

$$\frac{dD_j}{dt} = \frac{D_0 - D_j}{\tau_D} - \alpha_D \cdot D_j \cdot \delta(t - t_j). \tag{19}$$

Where the parameter $D_0 = 1$ sets the maximum value of D_j, $\tau_D = 1000\,ms$ sets the rate of recovery from synaptic depression, $\alpha_D = 0.2$ sets the fractional depression of the synapse each time neuron j spikes and $\delta(.)$ is the Kronecker delta function which equals one at the time of each spike in neuron j and zero otherwise. Parameters were chosen to qualitatively match data from (4).

Network construction. The preBötC network was constructed with random synaptic connectivity distribution where the connection probability of $P_{Syn} = 13\%$ as motivated by available experimental estimates (10). The weights of excitatory conductances were uniformly distributed such that $W_{j,i} = U(0, W_{Max})$, where $W_{Max} = 0.2\,nS$ is the maximal synaptic conductance.

Heterogeneity of intrinsic cellular properties was introduced into the network by normally distributing the parameters g_{leak} and g_{NaP} (Table S1) as well as by uniformly distributing g_{SPK} in Figs. 4–7 to introduce spike amplitude variability. The *leak* and NaP conductances were conditionally distributed in order to achieve a bivariate normal distribution, as suggested by (11, 12). In our simulations, this was achieved by first normally distributing g_{NaP} in each neuron according to the values presented in Table S1. Then a property of bivariate normal distribution was used which says that the conditional distribution of g_{leak} given g_{NaP} is itself a normal distribution with mean (μ^*_{Leak}) and standard deviation (σ^*_{Leak}) described as follows:

$$\mu^*_{Leak} = \mu_{Leak} + \rho \cdot (\sigma_{Leak}/\sigma_{NaP}) \cdot (g^i_{NaP} - \mu_{NaP}), \tag{20}$$

$$\sigma^*_{Leak} = \sqrt{(1 - \rho^2) \cdot \sigma^2_{Leak}} \tag{21}$$

In these equations, μ_{Leak} and μ_{NaP} are the mean and σ_{Leak} and σ_{NaP} are the standard deviation of the g_{Leak} and g_{NaP} distributions, while $\rho = 0.8$ represents the correlation coefficient and g^i_{NaP} represents the persistent sodium current conductance for the i^{th} neuron. All parameters are given in Table S1.

Simulating hypoxia. To simulate the combined effects of hypoxia, we imposed changes in $V_{1/2}^{Na}$ and elevated $[Na^+]_{in}$ that were each fit to a sigmoidal function. Because the shift in $V_{1/2}^{Na}$ occurs relatively rapidly (within $40s$) (13) and the resulting depolarization and increased spiking activity is expected to exacerbate $[Na^+]_{in}$ accumulation as the Na^+/K^+-ATPase pump becomes compromised, hypoxia was simulated as an initial change in $V_{1/2}^{Na}$ followed by accumulation of $[Na^+]_{in}$.

Simulating temperature dependent changes in gating time constants and membrane capacitance. The rate constants for channel gating change exponentially with temperature and is characterized by a Q10 temperature coefficient, which is a measure of the degree to which the rate of a biological process depends on temperature over 10°C (14). Q10 values commonly observed for rate constants of voltage-dependent gating dynamics typically range from 1 to 3 (15–17). For simplicity and feasibility of these experiments, we assumed a Q10 of 1.5 in all voltage-dependent channel rate constants (17, 18). The resulting scaling factor (SI Appendix, Fig. S12B) was then multiplied by all of the time constants of the voltage-dependent gating variables ($\tau_X(V)$, Eq. 13) as well as the time constants for the synaptic current (τ_{syn} in Eq. 18) and the rate of recovery from synaptic depression (τ_D, Eq. 19). In addition to changes in rate constants, cells also experience a temperature-dependent increase in surface area, leading to changes in capacitance (19–21) at a rate of approximately 0.3% per °C (22). As such, the model membrane capacitance was increased at a rate of 0.3% per °C (see Fig.7 & SI Appendix, Fig. S12C).

Data analysis and definitions. Data generated from simulations was post-processed in MATLAB software ver. R2020b (MathWorks, Natick, MA, USA). An action potential was defined to have occurred in a neuron when its membrane potential V_m increased through $-35mV$. Histograms of population activity were calculated as the number of action potentials per $20\,ms$ bin per neuron, with units of Hz. The amplitudes and frequency of network rhythms were determined by first identifying the peaks and then calculating the inverse of the interpeak interval from the population histograms. Burst initiation (Fig.3) was defined as the peak in I_{NaP} recovery of channel availability/inactivation (h_{NaP}). Quantification of spike amplitude and AHP as a function of g_{SPK}, g_{AHP}, or other parameter manipulations (as in Figs.5–7) was done with $g_{NaP} = 0\,nS$ to eliminate intrinsic bursting which would make quantification of AHP impossible. To quantify the percentage of the population that became active since the prior burst we counted the number of neurons in the population that spiked starting $500\,mS$ after the peak of one burst to $500\,ms$ after the peak of the next burst, except in cases where the burst duration was longer than $500\,ms$ in which case this window was manually extended.

Integration methods. All simulations were performed locally on an eight-core computer running the Ubuntu 20.04 operating system. Simulation software was custom written in C++ and compiled with g++ version 9.3.0. Numerical integration was performed using the first-order Euler method with a fixed step-size (Δt) of $0.025ms$. All model codes will be made freely available on GitHub upon publication of this work.

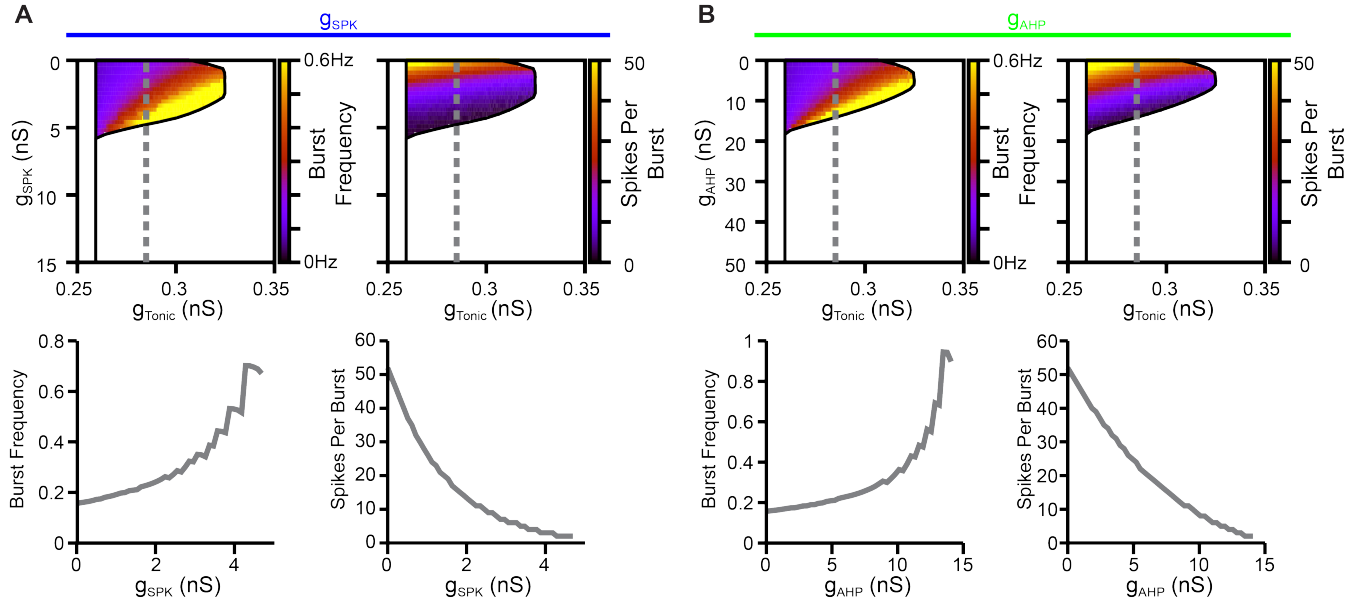

Fig. S1. Effect of changes in (A) g_{SPK} or (B) g_{AHP} on burst frequency (left) and the number of spikes per burst (right).

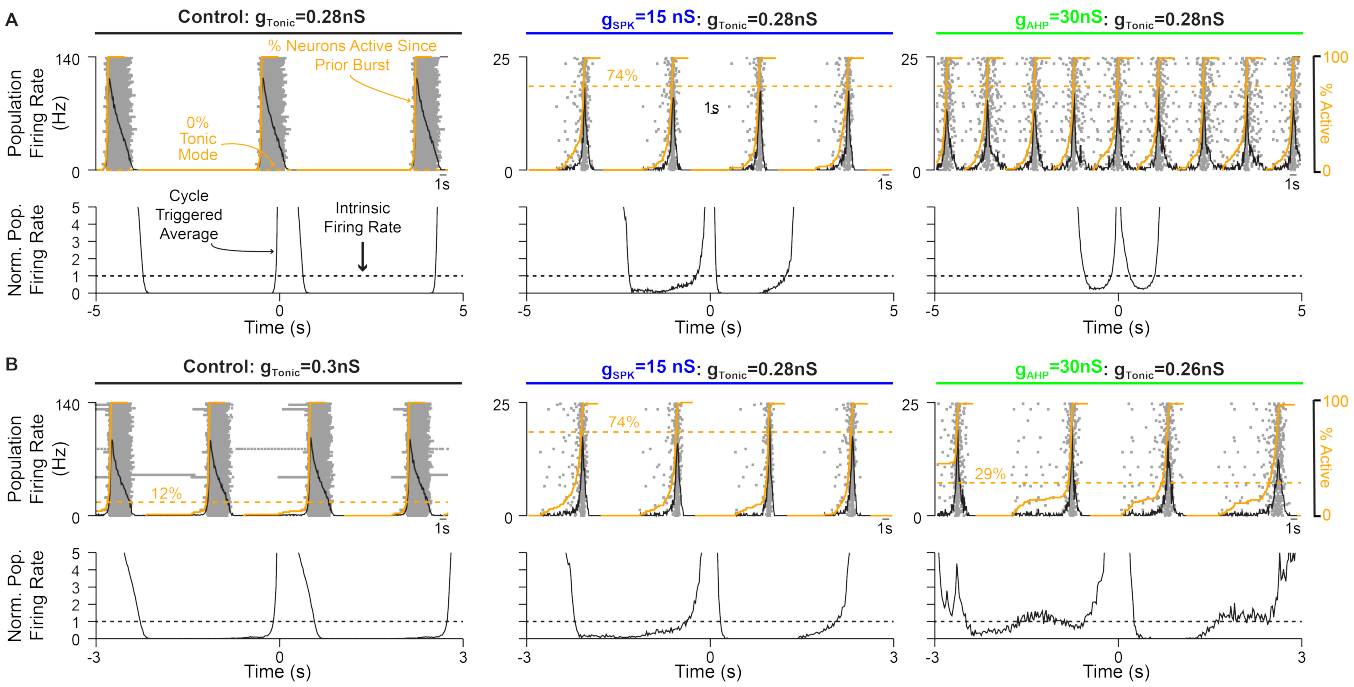

Fig. S2. Relationship between pre-inspiratory spiking, the percentage of neurons in tonic spiking mode and the intrinsic network firing rate. Example traces (top) and cycle triggered averages (bottom) in networks with (A) fixed excitability (g_{Tonic}) or (B) altered excitability such that network frequencies are roughly equal ($\approx 3\,Hz$). Horizontal yellow dashed line indicates the percentage of neurons in tonic spiking mode. The gray horizontal dashed line indicates the intrinsic network firing rate. Notice that the emergence of pre-inspiratory spiking coincides with the transition of neurons into tonic mode in the control network and in networks with altered spike shapes.

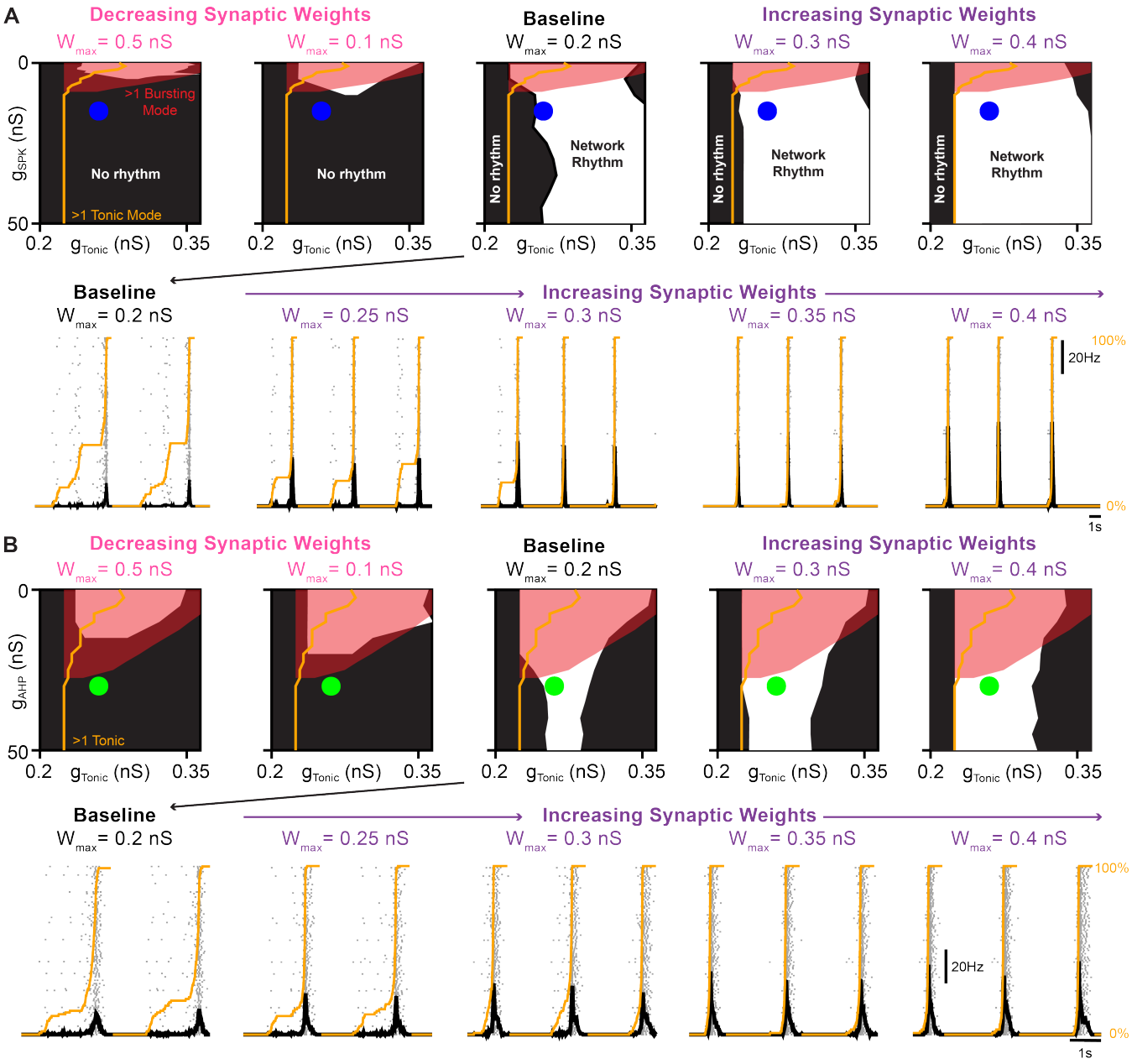

Fig. S3. Interactions between spike shape, intrinsic bursting, and synaptic weight for network rhythmogenesis. In networks with (A) altered g_{SPK} or (B) altered g_{AHP} the parameter space supporting network rhythmogensis (white regions) was collapsed by decreasing synaptic weights and expanded by increasing synaptic weights. Blue ($g_{AHP} = 30\,nS$) and green ($g_{SPK} = 15\,nS$) dots correspond to g_{SPK}/g_{AHP} and g_{Tonic} values of representative traces at baseline and during increasing synaptic weight. Orange lines in example traces indicate the percentage of neurons in the network that have become active since the preceding network burst.

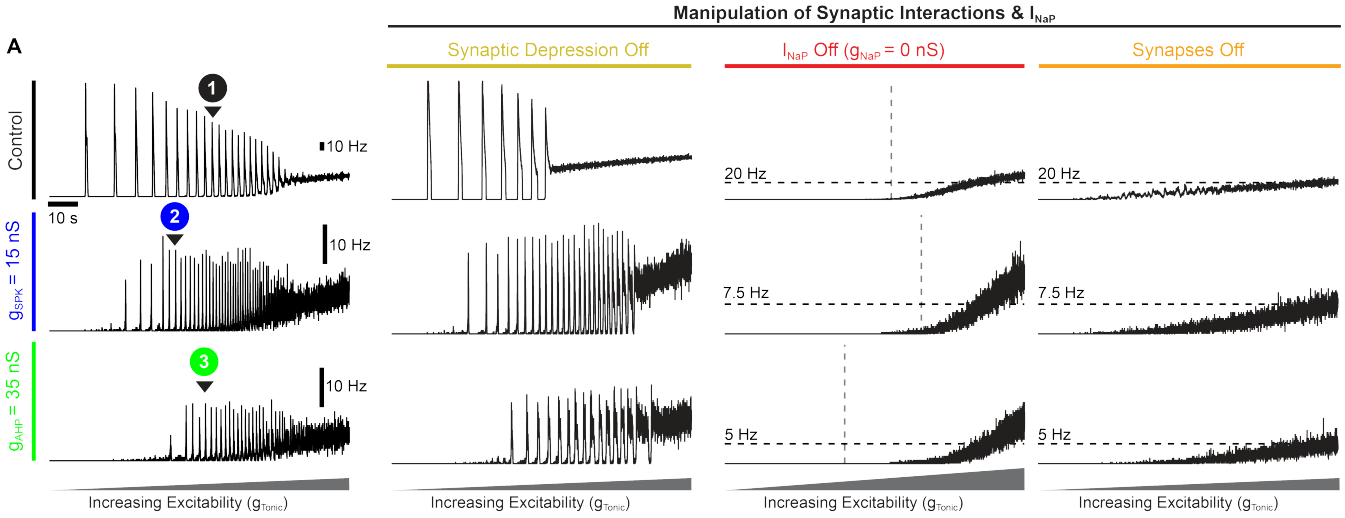

Fig. S4. Interdependence of I_{NaP} and synaptic interactions for network rhythmogenesis. (A) Activity of networks with all burst-capable (control) or burst-incapable ($g_{SPK} = 15\,nS$ or $g_{AHP} = 35\,nS$) neurons following elimination of synaptic depression, I_{NaP}, or all synaptic interactions. Notice, in the absence of synaptic depression, the excitability range supporting rhythmogenesis was substantially reduced in control networks with 100% burst-capable neurons but slightly increased in networks lacking intrinsic bursting.

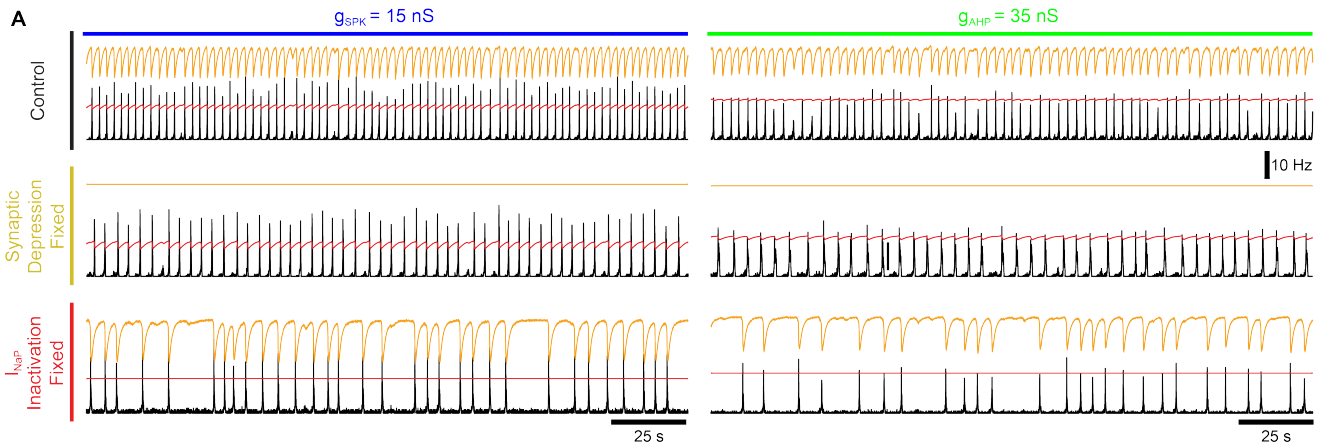

Fig. S5. Example network activity (firing rate) and corresponding synaptic depression (orange lines) and I_{NaP} inactivation (red lines) in networks with $g_{SPK} = 15\,nS$ (left) or $g_{AHP} = 35\,nS$ (right) under baseline conditions (top) or after fixing synaptic depression (middle) or I_{NaP} inactivation/availability (bottom). Notice the irregular network burst frequency that occurs when I_{NaP} inactivation/availability is fixed.

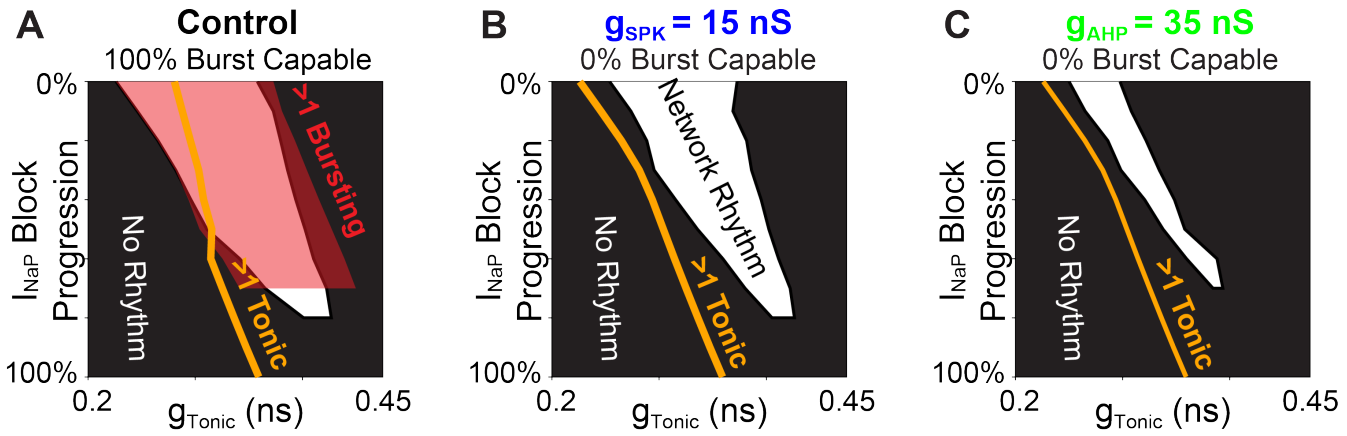

Fig. S6. Parameter space supporting intrinsic bursting (red) and network rhythmogenesis (white) as a function of excitability (g_{Tonic}) during progressive I_{NaP} block in (A) a control network with 100% of neurons initially burst capable ($g_{SPK} = g_{AHP} = 0$) and in networks with (B) $g_{SPK} = 15\,nS$ or (C) $g_{AHP} = 35nS$ to eliminate intrinsic bursting. Orange lines indicate g_{Tonic} value at which ≥ 1 neuron enters tonic spiking mode.

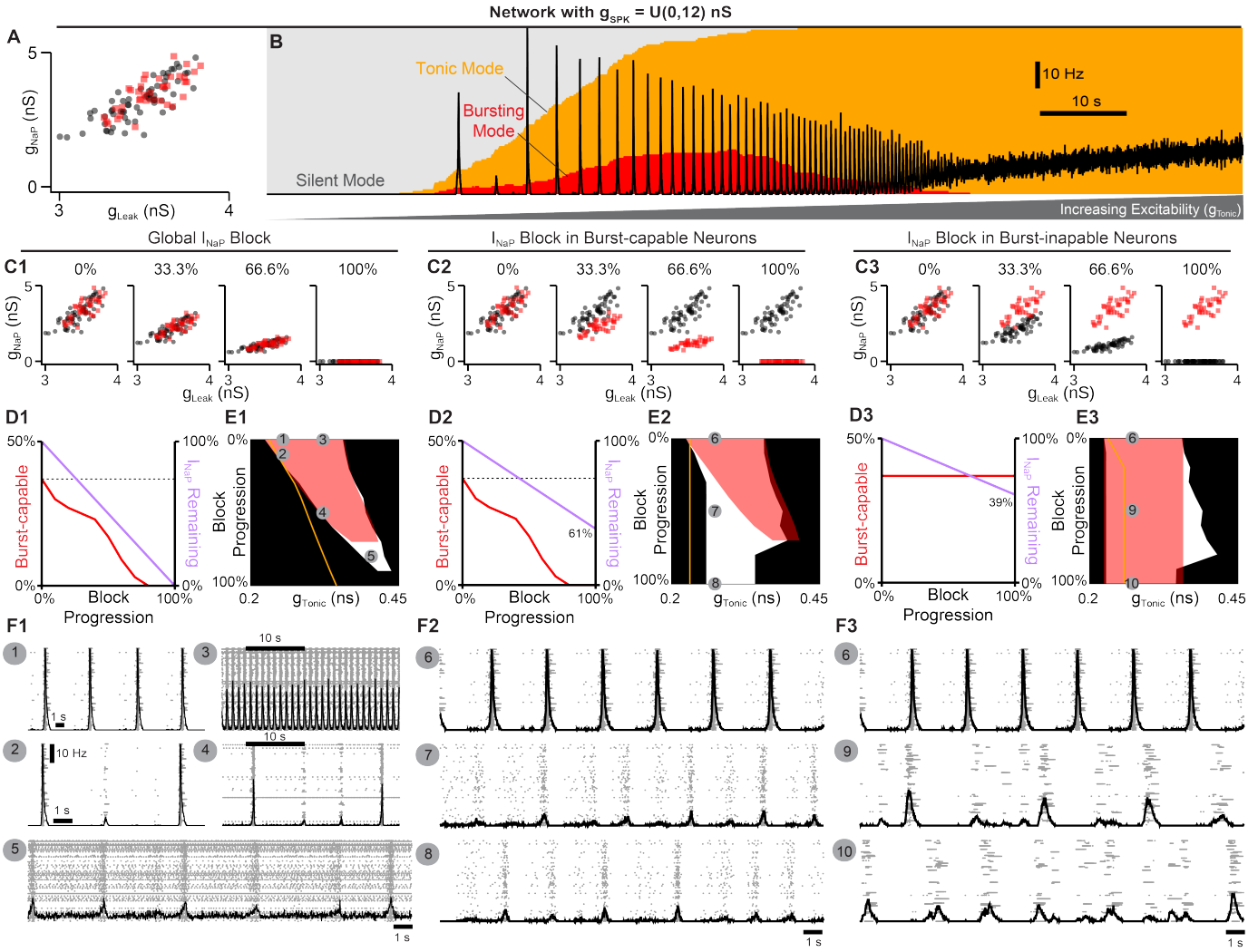

Fig. S7. Selective block of I_{NaP} in burst-capable or burst-incapable neurons has similar consequences for rhythm generation. (A) Distributions of g_{NaP} and g_{Leak} among burst-capable (red) and incapable (black) neurons in a network with $g_{SPK} = U(0, 12)\ nS$. (B) Prevalence of silent, bursting, and tonic intrinsic cellular activities with overlaid network firing rate during increasing g_{Tonic} in the same network. (C1-3) Comparison of global I_{NaP} block (C1) vs. progressive I_{NaP} block specifically in neurons that are initially burst-capable (C2) or burst-incapable (C3). (D1-3) Fraction of the network that is burst-capable and amount of I_{NaP} remaining as a function of I_{NaP} block progression. (E1-3) Parameter space supporting intrinsic bursting (red) and network rhythmogenesis (white) as a function of excitability (g_{Tonic}) during progressive I_{NaP} block. (F1-F3) Raster plots and overlaid network firing rate corresponding to points 1-10 shown in E1-3.

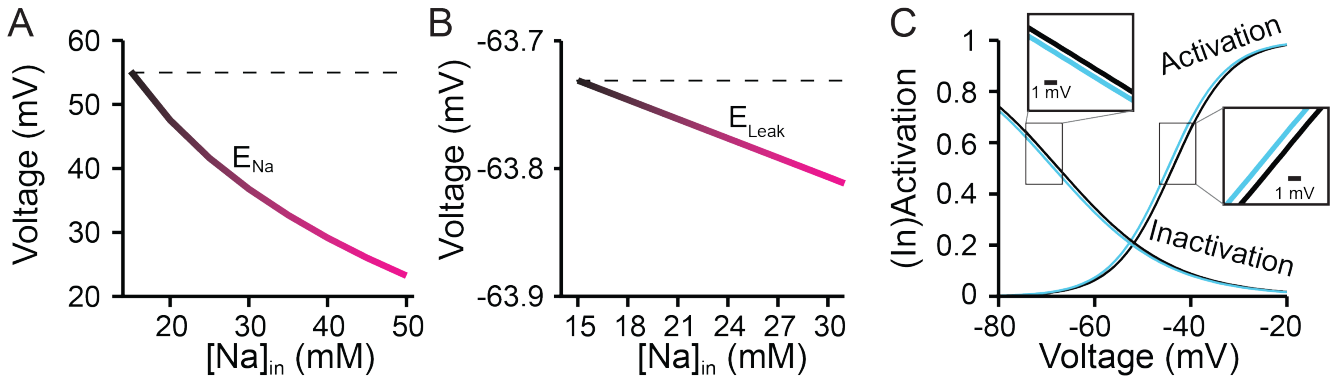

Fig. S8. Hypoxia related effects of accumulating $[Na^+]_{in}$ on (A) the sodium reversal potential and the (B) leak reversal potential. (C) Simulated hyperpolarizing shift in the (in)activation dynamics of spike generating sodium currents.

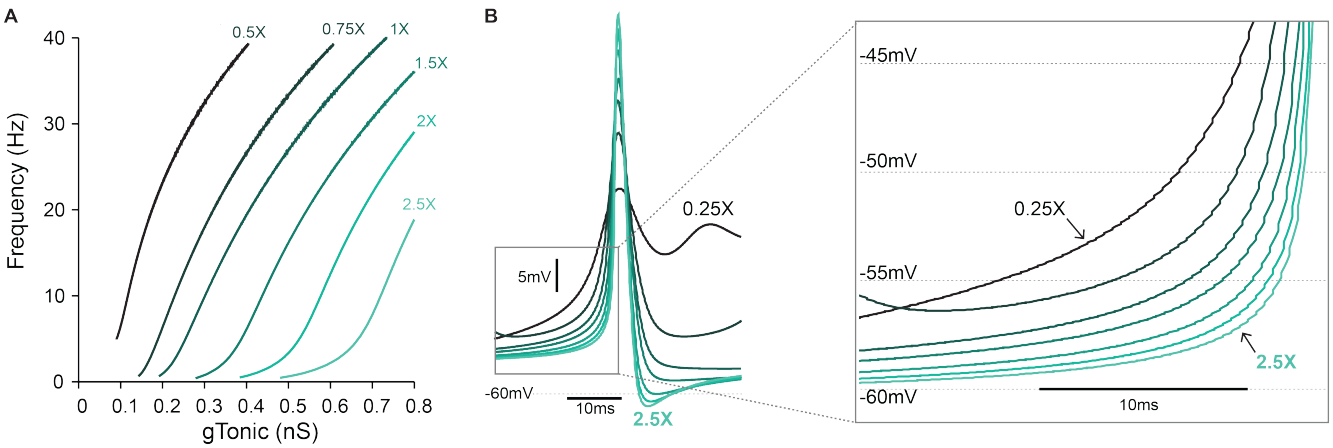

Fig. S9. Impact of conductance scaling on (A) the relationship between g_{Tonic} and firing rate and (B) the voltage "threshold" for spike generation.

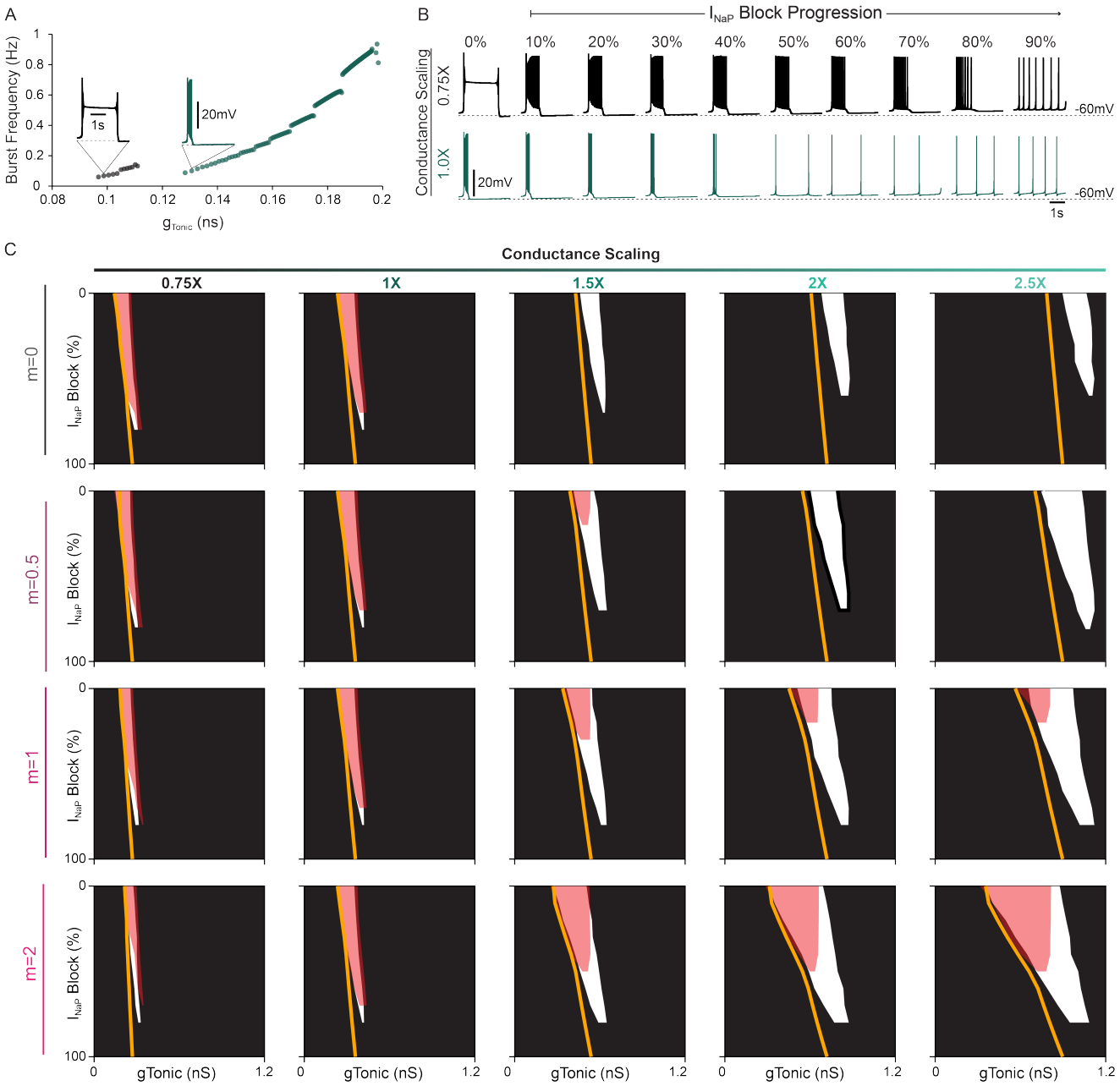

Fig. S10. (A) Relationship between excitability (g_{Tonic}) and burst frequency and (B) effect of simulated I_{NaP} block on intrinsic bursting capabilities for a neuron in with reduced conductance scaling (0.75X,m=1) compared to control scaling (1.0X,m=1). (C) Parameter space supporting network rhythmogenesis during progressive I_{NaP} block with scaled conductances.

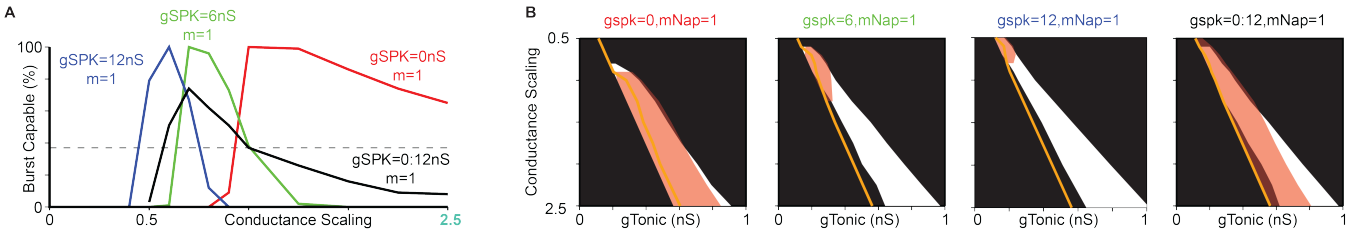

Fig. S11. Comparison of conductance scaling across networks with $g_{SPK} = 0\,nS$, $g_{SPK} = 6\,nS$, $g_{SPK} = 12\,nS$, or $g_{SPK} = U(0, 12)\,nS$ showing (A) fraction of the network that is burst-capable, and (B) parameter spaces supporting intrinsic bursting (red) and network rhythmogenesis (white) as conductances are up- or down-scaled (Orange lines indicate g_{Tonic} where ≥ 1 neuron enters tonic spiking mode).

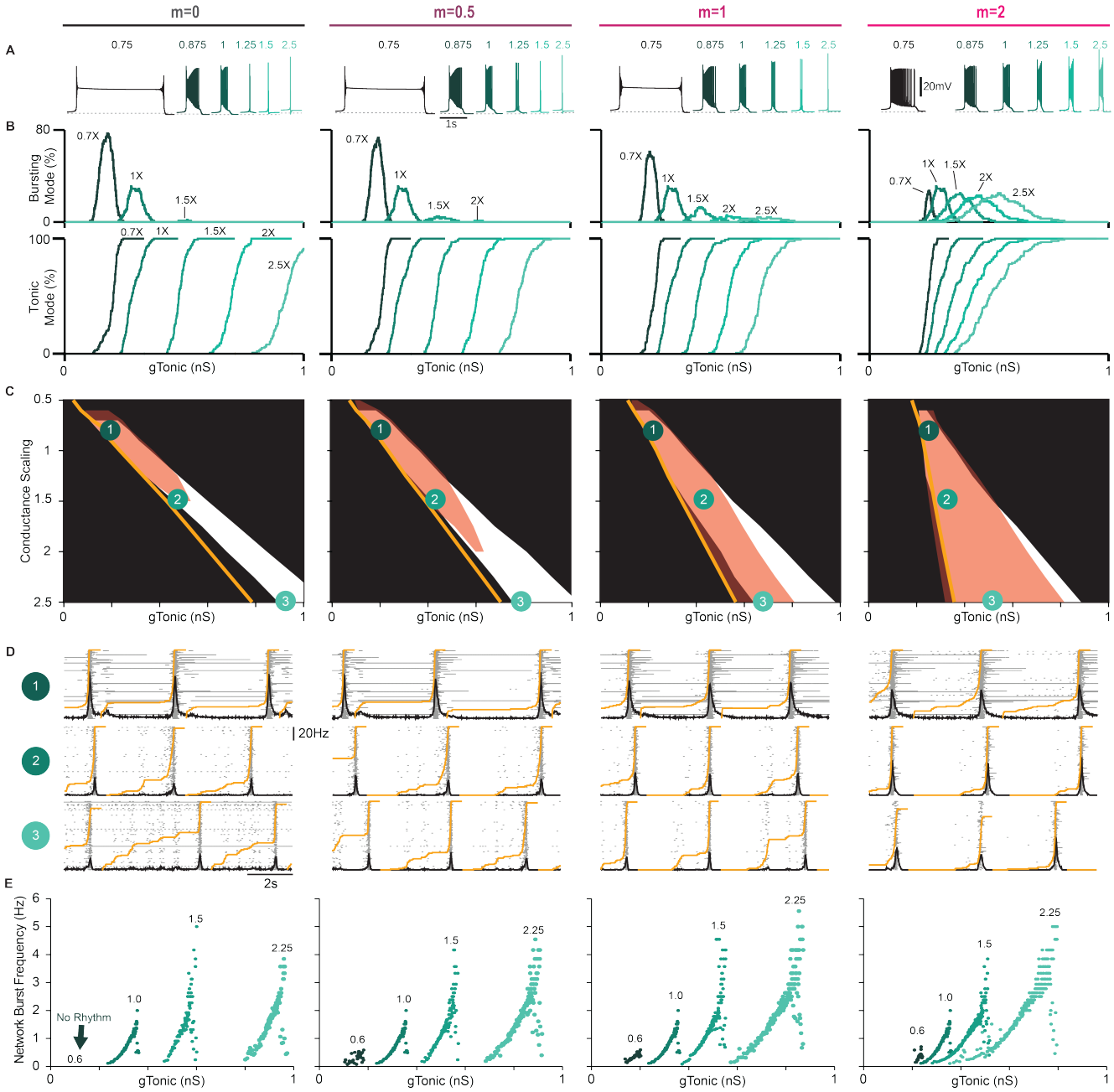

Fig. S12. (A) Example intrinsic bursting neurons during conductance scaling with $m = 0 - 2$. (B) Decreased excitability with conductance scaling as indicated by a rightward shift in the level of g_{Tonic} needed to initiate intrinsic bursting or tonic spiking. (C) Comparison of parameter space that supports intrinsic bursting (red) and network rhythmogenesis (white) as conductances are scaled with m ranging from $0 - 2$ (Orange lines indicate g_{Tonic} where ≥ 1 neuron enters tonic spiking mode). (D) Raster plots and overlaid network firing rate corresponding to points 1-3 in (C) (Orange line indicate the percentage of neurons active since the preceding network burst). (E) Relationship between excitability (g_{Tonic}) and network burst frequency as conductances are scaled with m ranging from $0 - 2$.

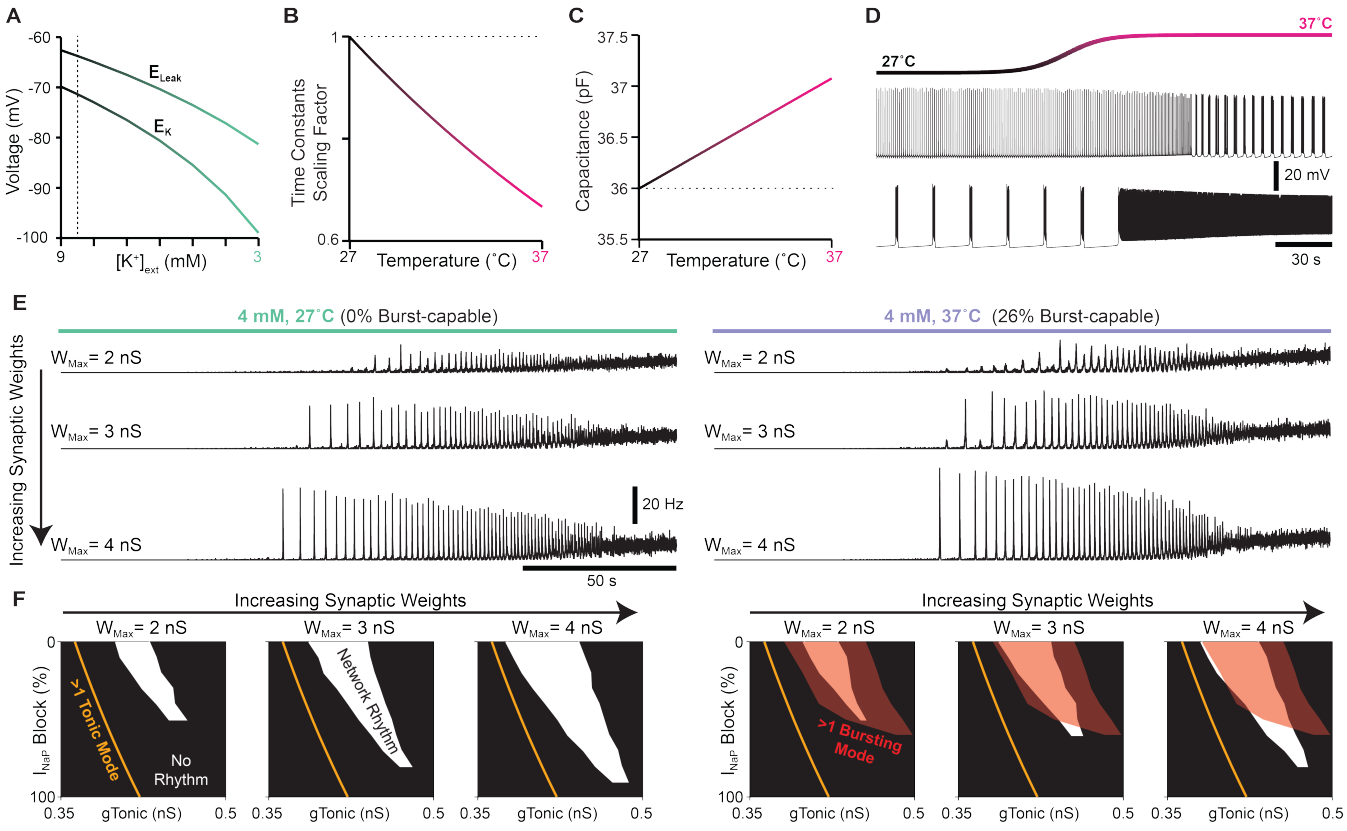

Fig. S13. Impact of extracellular potassium, temperature and synaptic weights on network properties and dynamics. (A) Relationship between the potassium (E_K) and leak (E_{Leak}) reversal potentials and extracellular potassium $[K^+]_{ext}$. Relationship between the scaling of time constants (B) and cellular capacitance (C) and the imposed temperature. (D) Example voltage traces illustrating the transition of a neuron from tonic to bursting mode and from bursting to tonic mode in response to an increase in temperature. (E) Effect of increases in synaptic weights on the network rhythm at physiological potassium and *in vitro* (left) or *in vivo* (right) temperatures. (F) Simulated I_{NaP} attenuation on network rhythms and intrinsic bursting.

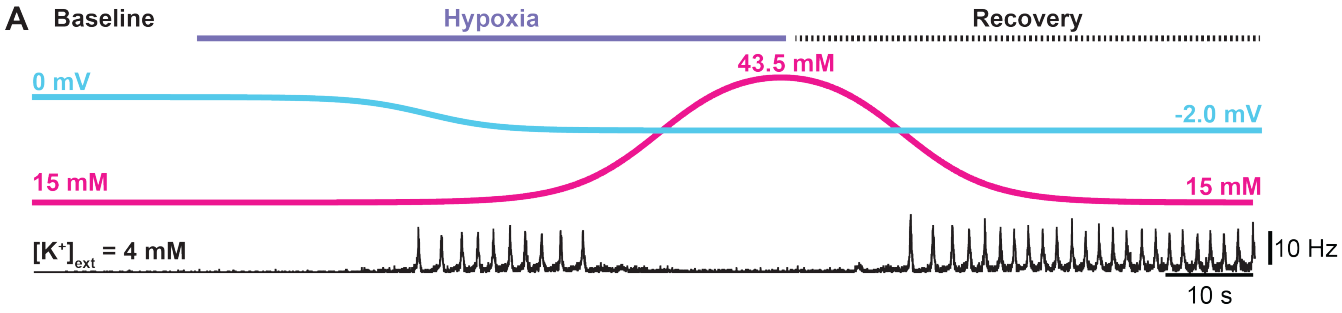

Fig. S14. Simulated hypoxia at physiological $[K^+]_{ext}$. (A) Network rhythm during transient hypoxia and recovery.

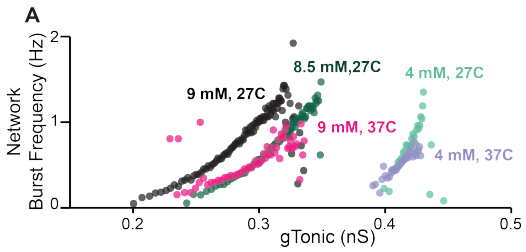

Fig. S15. (A) Effects of $[K^+]_{ext}$ and/or temperature on the relationship between excitability and network burst frequency.

References

1. PE Jasinski, YI Molkov, NA Shevtsova, JC Smith, IA Rybak, Sodium and calcium mechanisms of rhythmic bursting in excitatory neural networks of the pre-b ötzinger complex: a computational modelling study. *Eur. J. Neurosci.* **37**, 212–230 (2013).
2. RS Phillips, TT John, H Koizumi, YI Molkov, JC Smith, Biophysical mechanisms in the mammalian respiratory oscillator re-examined with a new data-driven computational model. *Elife* **8**, e41555 (2019).
3. RS Phillips, JE Rubin, Effects of persistent sodium current blockade in respiratory circuits depend on the pharmacological mechanism of action and network dynamics. *PLoS computational biology* **15**, e1006938 (2019).
4. A Kottick, CA Del Negro, Synaptic depression influences inspiratory–expiratory phase transition in dbx1 interneurons of the prebötzinger complex in neonatal mice. *J. Neurosci.* **35**, 11606–11611 (2015).
5. JE Rubin, JA Hayes, JL Mendenhall, CA Del Negro, Calcium-activated nonspecific cation current and synaptic depression promote network-dependent burst oscillations. *Proc. Natl. Acad. Sci.* **106**, 2939–2944 (2009).
6. C Guerrier, JA Hayes, G Fortin, D Holcman, Robust network oscillations during mammalian respiratory rhythm generation driven by synaptic dynamics. *Proc. Natl. Acad. Sci.* **112**, 9728–9733 (2015).
7. LF Abbott, J Varela, K Sen, S Nelson, Synaptic depression and cortical gain control. *Science* **275**, 221–224 (1997).
8. P Dayan, LF Abbott, *Theoretical neuroscience: computational and mathematical modeling of neural systems*. (Computational Neuroscience Series), (2001).
9. A Morrison, M Diesmann, W Gerstner, Phenomenological models of synaptic plasticity based on spike timing. *Biol. cybernetics* **98**, 459–478 (2008).
10. JC Rekling, XM Shao, JL Feldman, Electrical coupling and excitatory synaptic transmission between rhythmogenic respiratory neurons in the prebötzinger complex. *J. Neurosci.* **20**, RC113–RC113 (2000).
11. CA Del Negro, N Koshiya, RJ Butera Jr, JC Smith, Persistent sodium current, membrane properties and bursting behavior of pre-botzinger complex inspiratory neurons in vitro. *J. neurophysiology* **88**, 2242–2250 (2002).
12. H Koizumi, JC Smith, Persistent na+ and k+-dominated leak currents contribute to respiratory rhythm generation in the pre-bötzinger complex in vitro. *J. Neurosci.* **28**, 1773–1785 (2008).
13. LD Plant, JD Marks, SA Goldstein, Sumoylation of nav1. 2 channels mediates the early response to acute hypoxia in central neurons. *Elife* **5**, e20054 (2016).
14. DC Sterratt, Q10: the effect of temperature on ion channel kinetics in *Encyclopedia of Computational Neuroscience*. (Springer New York), pp. 2551–2552 (2015).
15. CA Collins, E Rojas, Temperature dependence of the sodium channel gating kinetics in the node of ranvier. *Q. J. Exp. Physiol. Transl. Integration* **67**, 41–55 (1982).
16. JF Fohlmeister, ED Cohen, EA Newman, Mechanisms and distribution of ion channels in retinal ganglion cells: using temperature as an independent variable. *J. neurophysiology* **103**, 1357–1374 (2010).
17. Y Yu, AP Hill, DA McCormick, Warm body temperature facilitates energy efficient cortical action potentials. *PLoS computational biology* **8**, e1002456 (2012).
18. JS Caplan, AH Williams, E Marder, Many parameter sets in a multicompartment model oscillator are robust to temperature perturbations. *J. Neurosci.* **34**, 4963–4975 (2014).
19. MG Shapiro, K Homma, S Villarreal, CP Richter, F Bezanilla, Infrared light excites cells by changing their electrical capacitance. *Nat. communications* **3**, 736 (2012).
20. B Pinto, CAZ Bassetto Jr, R Latorre, F Bezanilla, Measuring temperature time course using membrane capacitance. *Biophys. J.* **120**, 240a (2021).
21. BI Pinto, CA Bassetto Jr, F Bezanilla, Optocapacitance: physical basis and its application. *Biophys. Rev.* **14**, 569–577 (2022).
22. M Plaksin, E Shapira, E Kimmel, S Shoham, Thermal transients excite neurons through universal intramembrane mechanoelectrical effects. *Phys. Rev. X* **8**, 011043 (2018).